American Mineralogist, Volume 91, pages 1240–1248, 2006

Site preference and local geometry of Sc in garnets: Part II. The crystal-chemistry of octahedral Sc in the andradite–$Ca_3Sc_2Si_3O_{12}$ join

Simona Quartieri,[1,*] Roberta Oberti,[2] Massimo Boiocchi,[3] Maria Chiara Dalconi,[1,†] Federico Boscherini,[4] Olga Safonova,[5] and Alan B. Woodland[6]

[1]Dipartimento di Scienze della Terra, Università di Messina, Salita Sperone 31, I-98166 Messina S. Agata, Italy
[2]CNR, Istituto di Geoscienze e Georisorse, Unità di Pavia, via Ferrata 1, I-27100 Pavia, Italy
[3]Centro Grandi Strumenti, Università di Pavia, via Bassi 21, I-27100 Pavia, Italy
[4]Dipartimento di Fisica and CNISM, Università di Bologna, Viale Berti Pichat 6/2, I-40127 Bologna, Italy
[5]European Synchrotron Radiation Facility, 6 rue Jules Horowitz, BP 220, F-38043 Grenoble Cedex, France
[6]Institut für Mineralogie, Universität Frankfurt, Senckenberganlage 30, D-60054 Frankfurt, Germany

Abstract

Investigation of scandium incorporation in garnets along the synthetic $Ca_3Fe_2^{3+}Si_3O_{12}$–$Ca_3Sc_2Si_3O_{12}$ (adr–CaSc) join, based on the same multi-technique approach used in the companion paper (Oberti et al. 2006a), shows that (1) Sc is incorporated exclusively at the Y octahedron; (2) the local coordination of Sc is slightly different in Sc-poor than in Sc-rich compositions (Sc-O = 2.06 Å in $CaSc_{10}$ vs. 2.10 Å in $CaSc_{30–90}$); (3) the local coordination of Ca is also slightly different in Sc-poor than in Sc-rich compositions [Ca1,2-O are 2.34(2) and 2.48(2) Å in $CaSc_{10}$ and 2.36(2) and 2.50(2) Å in $CaSc_{90}$, with Δ fixed at 0.14 Å in all the samples]; (4) the linear increase of the unit-cell edge along the join derives from multiple changes in the geometry of the different polyhedra and from the rotation of the tetrahedron around the $\bar{4}$ axis (α rotation), and cannot be modeled from extrapolation of the behavior observed along the $Ca_3Al_2Si_3O_{12}$–$Ca_3Fe_2^{3+}Si_3O_{12}$ (grs–adr) join.

CaSc-rich garnets, where a large X dodecahedron coexists with a large Y octahedron and a Z tetrahedron occupied by Si, similar to pyrope-grossular garnets, have the highest α values observed to date in calcium silicate garnets. Slightly lower α values are observed in pyrope and almandine, but correspond to a different structural arrangement, where a small X dodecahedron coexists with a small Y octahedron. These results further confirm the efficiency of a combined short- and long-range approach for understanding the properties of garnet solid solutions.

Keywords: Crystal structure, garnet, XAS, XRD data, trace elements and REE, scandium, crystal synthesis

Introduction

Investigation of Sc incorporation and partitioning in pyrope–grossular (prp–grs) garnet solid solutions has revealed variable crystal-chemical behavior. Oberti et al. (2006a) found that Sc enters the dodecahedral X site in the very compact structure of pyrope, but partitions itself among all the available structural sites when the presence of Ca allows local relaxation. Notably, Sc incorporation at the octahedral Y site never exceeds 0.20 atoms per formula unit (apfu) in the prp–grs join. This contrasts with the nearly ideal volumes of mixing found by Woodland and Angel (1996a, 1996b) along the (synthetic) $Ca_3Fe_2^{3+}Si_3O_{12}$–$Ca_3Sc_2Si_3O_{12}$ (adr–CaSc) join. In these binary compositions, electron microprobe and X-ray powder diffraction analyses indicated that Sc regularly substitutes for Fe^{3+} at the Y site.

The samples investigated by Woodland and Angel (1996a, 1996b) were therefore examined by single-crystal structure refinement (SREF) and X-ray absorption spectroscopy (XAS) to obtain a complete long- and short-range characterization of the Sc Fe^{3+}_{-1} exchange in garnets, and to detect possible structural constraints that may limit Sc incorporation in garnet compositions that possess more compact structures.

Experimental details

Synthesis

End-member $Ca_3Sc_2Si_3O_{12}$ garnet was synthesized from a stoichiometric mixture of high purity oxides in air at 1 bar and 1000 °C using a K_2O-B_2O_3 (45 wt% K_2O) flux. The oxide mixture was combined with the flux in a 75:25 ratio. The sample crucible was quenched in water in a way to avoid direct water contact with the sample. The result was a mass of small equant colorless crystals that were separated from the flux by soaking in nitric acid.

Binary $Ca_3Fe_2Si_3O_{12}$–$Ca_3Sc_2Si_3O_{12}$ solid solutions were produced in a piston-cylinder apparatus at the Bayerisches Geoinstitut, Germany using stoichiometric mixtures of $CaSiO_3$, Fe_2O_3, and Sc_2O_3. The $CaSiO_3$ was pre-synthesized by sintering an equimolar mixture of $CaCO_3$ and SiO_2 at 1 bar and 1200 °C for 12 h. The syntheses were performed without any flux at 2.0 GPa and 1000 °C, using silver capsules and talc-pyrex pressure cells. Details of the pressure calibration are given in Woodland and O'Neill (1995). The duration of the experiments was approximately 24 h.

Electron microprobe and Mössbauer analysis

Chemical compositions were determined using a Cameca SX-50 electron microprobe (EMP) at the Mineralogisches Institut, Universität Heidelberg, Germany.

* E-mail: simonaq@unimo.it
† Present address: Dipartimento di Scienze della Terra, Università di Ferrara, via Saragat 1, I-44100 Ferrara, Italy

Operating conditions were 15 kV and 20 nA in wavelength dispersive mode, using various synthetic and natural standards and counting for 20 or 30 s each on the peak and background (PAP correction procedure by Pouchou and Pichoir 1985).

Sample compositions are presented in Table 1. For the end-member $Ca_3Sc_2Si_3O_{12}$ garnet, which was synthesized in the K_2O-B_2O_3 flux, peak searches and wavelength scans failed to detect any B and K, thus confirming the nominal composition.

All solid solutions were analyzed by Mössbauer spectroscopy to verify the valence and coordination of the Fe present. The samples were finely ground and mounted on thin plastic film using polyvinyl alcohol. Spectra were obtained at the Bayerisches Geoinstitut at room temperature, in transmission mode on a constant acceleration Mössbauer spectrometer with a nominal 50 mCi ^{57}Co source in a 6 μm Rh matrix. The velocity scale was calibrated relative to 25 μm thick α-Fe at room temperature using the positions certified by NIST. Mirror image spectra were collected over 512 channels with a velocity range of ±5 mm/s. The spectra were folded and fit with the NORMOS software package (distributed by Wissenschaftliche Elektronik GmbH, Germany).

Mössbauer spectra generally exhibited a single doublet with hyperfine parameters consistent with Fe^{3+} in octahedral coordination (Fig. 1, and see Amthauer et al. 1976; Woodland and Ross 1994). The hyperfine parameters and peak widths remain constant across the join, indicating that the chemical environment of Fe^{3+} is essentially unaffected by the progressive substitution of Sc (Table 2). This behavior is similar to that observed for the octahedrally coordinated Fe^{3+} in $Fe^{2+}_3Al_2Si_3O_{12}$– $Fe^{2+}_3Fe^{3+}_2Si_3O_{12}$ garnets, and supports the notion that the neighboring octahedra in the garnet structure are too distant from each other for significant electronic interactions to occur between these sites (Woodland and Ross 1994). In three samples, Mössbauer spectra revealed an additional, very small doublet corresponding to Fe^{2+} on the dodecahedral sites (e.g., Fig. 1). This implies that these garnets contain traces of $Fe^{2+}_3Fe^{3+}_2Si_3O_{12}$ or "skiagite" component so that they deviate slightly from true $Ca_3Fe_2Si_3O_{12}$–$Ca_3Sc_2Si_3O_{12}$ binary compositions. However, the derived skiagite contents amount to no more than 1.5 mol% (Table 1) and, for such small quantities, we can reliably make a linear correction to the unit-cell parameter to compensate for this minor component.

X-ray analysis and structure refinement

X-ray powder diffraction (XRPD) patterns in the range of 30 to 120° 2θ were recorded for all samples on a Stoe STADI-P diffractometer equipped with a Co X-ray source, a monochromator aligned to yield Co$K\alpha_1$ radiation, and a small-aperture linear PSD. Si metal was used as an internal standard. Unit-cell parameters were determined with the Rietveld whole-pattern method using the EXPGUI-GSAS software package (Toby 2001; Larson and Von Dreele 1997).

The measured cell parameter of $Ca_3Sc_2Si_3O_{12}$ [a = 12.2451(3) Å] is slightly larger than that reported by Ito and Frondel (1968) [a = 12.23(1)Å], but tendentially smaller than that reported by Mill et al. 1977 [a = 12.250 (2)]. For the adr–CaSc solid solutions, most samples were found to be single phase except for two samples, $adr_{80}CaSc_{20}$ and $adr_{50}CaSc_{50}$, which were found to contain traces of clinopyroxene.

Single-crystal X-ray diffraction data were collected at the maximum resolution allowed by crystal dimensions at the CNR-IGG (Pavia) with a Bruker-AXS Smart-Apex CCD-based diffractometer, working with graphite monochromatized Mo$K\alpha$ radiation at 55 kV and 30 mA. Omega rotation frames were collected using the SMART software (Bruker-AXS Inc.). Data reduction (including intensity integration, background, Lorentz, and polarization corrections) was performed with the SAINT software (Bruker-AXS Inc.). Absorption effects were evaluated using the SADABS software (Sheldrick 1996), and absorption correction was applied to the data. The unit-cell edge was obtained after data reduction from least-squares refinements of the centroid of gravity of all the collected reflections.

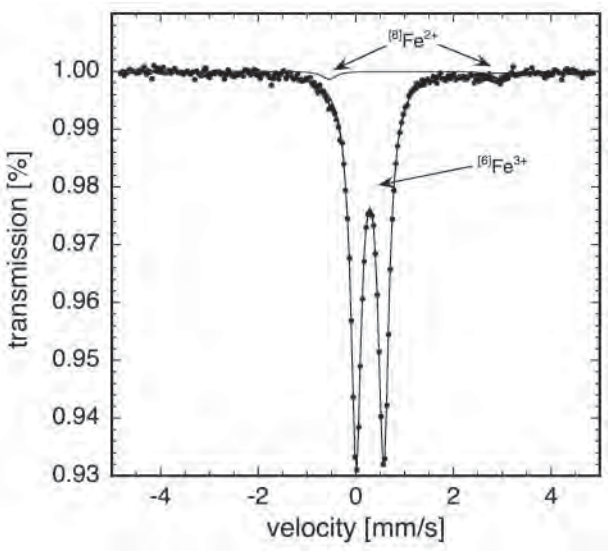

FIGURE 1. A typical Mössbauer spectrum for the solid solution term in the adr–CaSc join, which also shows the presence of a very small skiagite component.

TABLE 2. Mössbauer hyperfine parameters

Sample	X_{CaSc}	Fe^{3+}		FWHM
		CS*	QS*	
adr_{100} aw63†		0.40	0.55	0.25
$adr_{90}CaSc_{10}$	0.10(1)	0.40	0.56	0.26
$adr_{80}CaSc_{20}$	0.217(15)	0.40	0.56	0.26
$adr_{70}CaSc_{30}$	0.28(2)	0.40	0.56	0.26
$adr_{50}CaSc_{50}$	0.50(1)	0.40	0.58	0.27
$adr_{30}CaSc_{70}$	0.69(1)	0.41	0.57	0.29

* mm/s measured relative to α-Fe metal at 298 K.
† From Woodland and Ross (1994).

TABLE 1. Sample codes and unit formulae for the samples of this work

Nom. comp.	adr_{100}	$adr_{90}CaSc_{10}$	$adr_{80}CaSc_{20}$	$adr_{70}CaSc_{30}$	$adr_{50}CaSc_{50}$	$adr_{30}CaSc_{70}$	$adr_{10}CaSc_{90}$90	$CaSc_{100}$‖
Code	aw63	aw139	aw139	aw138	aw138	aw138	aw139	csgt2
No.*	†	30	19	17	40	17	22	9
SiO_2 (wt%)	35.95	35.22(11)	35.77(12)	36.06(8)	36.14(7)	36.76(18)	37.46(9)	34.75(45)
Sc_2O_3	–	2.71(43)	5.94(45)	7.82(41)	13.93(37)	19.20(31)	24.83(28)	29.11(22)
FeO	28.31	26.40(47)	22.95(54)	21.01(48)	14.57(34)	9.02(31)	3.26(24)	–
CaO	33.42	32.46(12)	32.95(14)	33.14(15)	33.65(17)	34.07(15)	34.79(13)	34.42(29)
Total	97.68	96.79(24)	97.69(28)	98.05(45)	98.29(21)	99.35(30)	100.34(25)	98.38(30)
$Fe^{3+}/\Sigma Fe$‡	1.0	0.978	1.0	0.975	~0.99	1.0	1.0	–
Formulae based on 12 oxygen atoms								
Si	3.013	2.979(8)	2.992(6)	3.001(5)	2.994(5)	3.012(14)	3.022(5)	2.887(23)
Sc	–	0.200(31)	0.433(31)	0.567(29)	1.005(24)	1.371(20)	1.746(17)	2.108(21)
$^{[6]}Fe^{3+}$‡	1.985	1.826(34)	1.607(35)	1.424(33)	1.000(23)	0.618(21)	0.222(14)	–
$^{[8]}Fe^{2+}$‡		0.041	–	0.038	0.010	–	–	–
Ca	3.002	2.941(10)	2.952(12)	2.954(10)	2.989(9)	2.991(10)	3.007(9)	3.064(30)
X_{Ski}§	0	0.014	0	0.013	0.003	0	0	0

* Number of points analyzed.
† From Woodland and O'Neill (1995).
‡ From Mössbauer spectroscopy.
§ mol% of the skiagite ($Fe^{2+}_3Fe^{3+}_2Si_3O_{12}$) component.
‖ From Mill et al. (1977).

TABLE 3. Selected results of the XRD analysis for the samples of this work

Sample	*a* SREF (Å)	*a* PWD (Å)*	*a* PWD_{corr} (Å)*	R_{all} (%)	X_{CaSc} probe	X_{CaSc} SREF	ss(Y) (epfu)	*x*(O)	*y*(O)	*z*(O)	B_{eq}(O) ($Å^2$)
adr_{100}†	12.0578(2)	12.0596(2)		2.7	–	0.00	52.03	0.03940(9)	0.04870(9)	0.65540(9)	0.50(1)
$adr_{90}CaSc_{10}$	12.0748(2)	12.0733(2)	12.0779	5.3	0.10(1)	0.10(1)	51.00(5)	0.03924(5)	0.04892(5)	0.65571(5)	0.40(1)
$adr_{80}CaSc_{20}$	12.0938(2)	12.0943(3)	–	3.3	0.217(15)	0.20(1)	50.00(5)	0.03945(5)	0.04890(5)	0.65598(5)	0.49(1)
$adr_{70}CaSc_{30}$	12.1128(2)	12.1123(1)	12.1163	2.8	0.28(2)	0.28(1)	49.16(5)	0.03950(5)	0.04910(5)	0.65636(5)	0.48(1)
$adr_{50}CaSc_{50}$	12.1493(2)	12.1520(2)	12.1536	3.2	0.50(1)	0.49(1)	47.10(5)	0.03965(5)	0.04935(5)	0.65696(5)	0.50(1)
$adr_{30}CaSc_{70}$	12.1917(2)	12.1906(2)	–	3.2	0.69(1)	0.68(1)	45.20(5)	0.03980(5)	0.04966(5)	0.65758(5)	0.51(1)
$adr_{10}CaSc_{90}$	12.2273(2)	12.2258(2)	–	3.6	0.87(1)	0.87(1)	43.32(1)	0.04004(5)	0.05005(5)	0.65812(5)	0.42(1)
$CaSc_{100}$‡	12.2500(20)	12.2455(4)	–	4.9	1.00	1.00	42.00	0.04004(24)	0.05010(23)	0.65887(24)	0.38

Sample	X1-O (Å)	X2-O (Å)	<X-O> (Å)	Δ X-O (Å)	Y-O (Å)	Z-O (Å)	sh X-X (Å)	unsh X (Å)	sh X-Y (Å)	unsh Y (Å)	sh X-T (Å)
adr_{100}†	2.361(1)	2.500(1)	2.431	0.139	2.020(1)	1.647(1)	2.933(1)	2.857(1)	2.881(1)	2.833(1)	2.566(1)
$adr_{90}CaSc_{10}$	2.362(1)	2.501(1)	2.432	0.139	2.027(1)	1.648(1)	2.928(1)	2.861(1)	2.887(1)	2.845(1)	2.565(1)
$adr_{80}CaSc_{20}$	2.366(1)	2.507(1)	2.436	0.141	2.034(1)	1.647(1)	2.932(1)	2.864(1)	2.899(1)	2.853(1)	2.563(1)
$adr_{70}CaSc_{30}$	2.369(1)	2.509(1)	2.439	0.140	2.042(1)	1.647(1)	2.929(1)	2.867(1)	2.910(1)	2.866(1)	2.561(1)
$adr_{50}CaSc_{50}$	2.375(1)	2.515(1)	2.445	0.140	2.056(1)	1.647(1)	2.929(1)	2.873(1)	2.930(1)	2.886(1)	2.559(1)
$adr_{30}CaSc_{70}$	2.382(1)	2.522(1)	2.452	0.140	2.072(1)	1.648(1)	2.928(1)	2.880(1)	2.951(1)	2.909(1)	2.558(1)
$adr_{10}CaSc_{90}$	2.389(1)	2.526(1)	2.458	0.137	2.086(1)	1.648(1)	2.926(1)	2.881(1)	2.972(1)	2.929(1)	2.559(1)
$CaSc_{100}$‡	2.390(3)	2.532(3)	2.461	0.142	2.099(3)	1.645(3)	2.921(4)	2.891(4)	2.989(4)	2.947(4)	2.548(4)

Notes: Abbreviations as specified in the text.
* Unit-cell edges by powder diffraction from Woodland and O'Neill (1995) corrected accordingly to their skiagite content ($Fe^{3+}_{3}Fe^{2+}_{2}Si_3O_{12}$), detected by Mössbauer spectroscopy (1.4, 1.2, and 0.5 mol% for the $adr_{90}CaSc_{10}$, $adr_{70}CaSc_{30}$, and $adr_{50}CaSc_{50}$ samples, respectively.
† From IGG-CNR (Pavia) database.
‡ From Mill et al. (1977).

In the case of $CaSc_{100}$, a crystal of suitable size for single-crystal analysis was not found in the relict material.

The unweighted full-matrix least-squares refinements (SREF) were done with a program locally developed to deal with complex solid solutions (Cannillo, personal communication) using scattering factors for fully ionized chemical species. The refinement was done using the *F* values of reflections with $I > 3\,\sigma(I)$. The results of the XRD analysis are given in Table 3.

XAS MEASUREMENTS AND DATA ANALYSIS

The XAS experiments were performed on three selected samples ($CaSc_{10}$, $CaSc_{30}$, and $CaSc_{90}$) at both the Ca and the Sc *K*-edges (4038 and 4492 eV, respectively) at the beamline ID26 of the European Synchrotron Radiation Facility (Grenoble, France).

Samples were prepared by grinding the garnet powders in a mortar to reduce the grain size, mixing them with cellulose and finally pressing them into 5 mm diameter pellets. XANES and EXAFS spectra were measured in the fluorescence mode using photo-diode detectors. Data acquisition was done at 40 K in the quick scan mode with synchronous movement of the undulator gap and the Bragg angle of the monochromator. About twenty scans were averaged for each sample.

XANES spectra were analyzed according to standard procedures. The pre-edge background was first subtracted from the raw XANES spectra. The spectra were then normalized on the high-energy side using a procedure that takes care of the effects resulting from the different sample thickness, and allows comparison of samples with different absorber contents.

The EXAFS signals were extracted from the experimental absorption spectra and analyzed using the interactive program IFEFFIT (Newville 2001) with the support of the graphical utilities ATHENA and ARTEMIS (Ravel and Newville 2005).

For the Sc *K*-edge data (Fig. 2), phase and amplitude back-scattering functions were calculated using the FEFF8 code (Ankudinov et al. 1998), placing the Sc absorber atoms at the octahedrally coordinated Y site. Coordination distances were derived from the XRD data for $Ca_3Sc_2Si_3O_{12}$ reported by Mill et al. (1977). The amplitude reduction factor ($S_0^2 = 1.0$) was obtained by fitting the data from sample Ca-Sc_{90} using the structural model from the $Ca_3Sc_2Si_3O_{12}$ end-member. Multiple-shell fits were done in *R* space $1.2 < R < 3.4$ Å with *k*-range $3.5 < k < 10.5$ $Å^{-1}$ by minimizing the difference between the raw data and the model EXAFS function (Table 4 and Fig. 3). The fitting parameters were a unique energy shift (ΔE_0) for all paths; two distinct mean-square displacement values (σ_i^2) for the oxygen shells and the non-oxygen paths (i.e., Ca and Si); two independent values of the path length (one for the oxygen shell and one for Ca and Si atoms occurring at the same distance).

For the Ca *K*-edge data (Fig. 4; $S_0^2 = 0.6$), a multiple-shell fit was done in the *R* space between 1.2 and 3.4 Å with a *k*-range $3.0 < k < 9.8$ $Å^{-1}$, using phase and back-scattering functions calculated for Ca absorber atoms occurring at the X

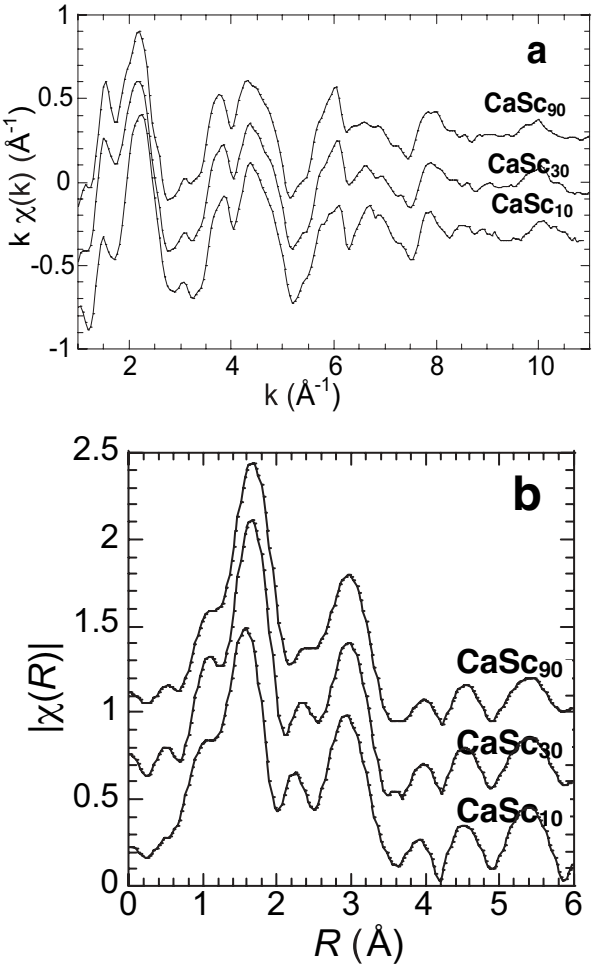

FIGURE 2. (**a**) Sc *K*-edge EXAFS data; (**b**) the corresponding Fourier transforms (k^2, $3.5 < k < 10.5$ $Å^{-1}$).

TABLE 3.—*EXTENDED*

B_{eq}(Z) ($Å^2$)	B_{eq}(Y) ($Å^2$)	B_{eq}(X) ($Å^2$)			
0.27(1)	0.35(1)	0.50(1)			
0.42(1)	0.36(1)	0.50(1)			
0.39(1)	0.39(1)	0.53(1)			
0.38(1)	0.37(1)	0.52(1)			
0.41(1)	0.39(1)	0.54(1)			
0.40(1)	0.39(1)	0.55(1)			
0.38(1)	0.36(1)	0.52(1)			
0.38	0.38	0.38			
unsh T (Å)	OAV ($°^2$)	X-X (Å)	X-Y (Å)	X-Z (Å)	α (°)
2.749(1)	0.99(6)	3.692(1)	3.370(1)	3.012(1)	27.24(5)
2.753(1)	0.77(6)	3.697(1)	3.375(1)	3.019(1)	27.42(5)
2.751(1)	0.93(6)	3.703(1)	3.380(1)	3.023(1)	27.48(5)
2.752(1)	0.85(6)	3.709(1)	3.386(1)	3.028(1)	27.67(5)
2.752(1)	0.82(6)	3.720(1)	3.396(1)	3.037(1)	27.94(5)
2.755(1)	0.77(6)	3.733(1)	3.408(1)	3.048(1)	28.25(5)
2.755(1)	0.75(6)	3.744(1)	3.418(1)	3.057(1)	28.58(5)
2.753(4)	0.69(12)	3.751(4)	3.424(4)	3.062(1)	28.80(10)

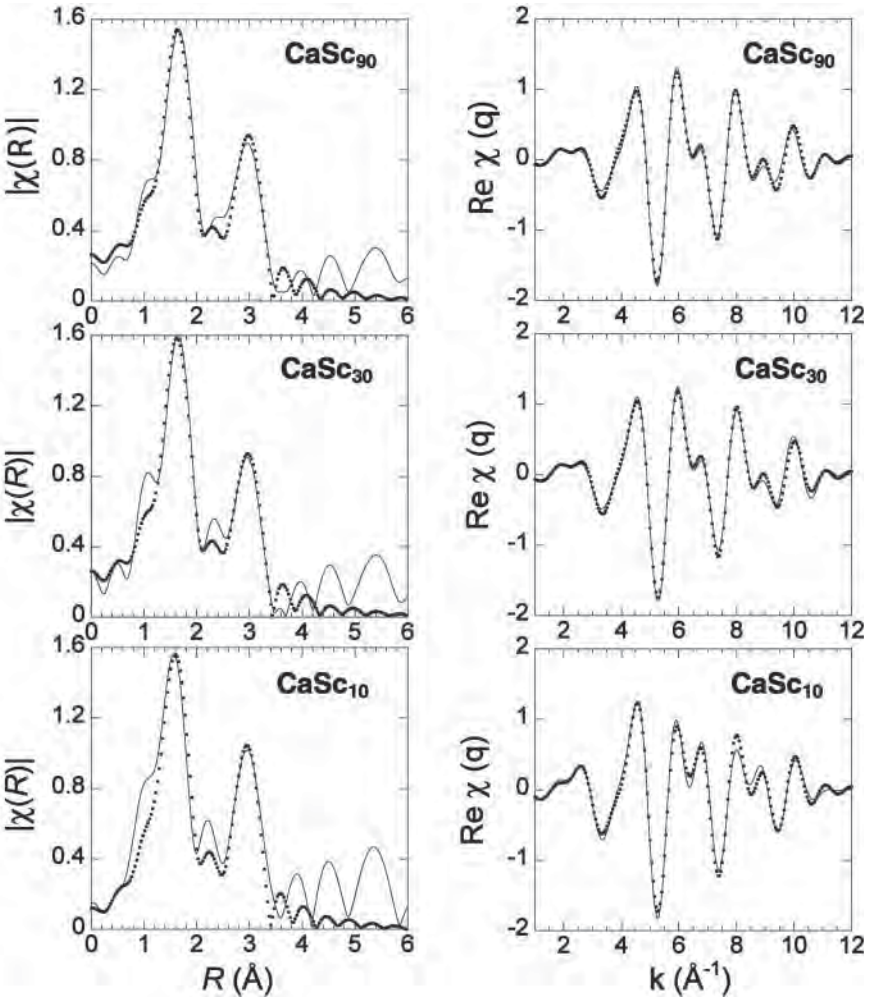

FIGURE 3. Left column: Fourier transform of Sc *K*-edge data (solid line) and fitted signal (dots) (*k*-weight = 2; *k*-range = 3.5–10.5 $Å^{-1}$); right column: inverse-Fourier transform of EXAFS data (solid line) and fitted signal (dots) ($1.2 < R < 3.4$ Å).

site. The fitting parameters were a unique energy shift (ΔE_0) for all paths, distinct mean-square displacement values (σ_i^2) for the two oxygen shells and one common σ_i^2 value for the non-oxygen paths, and four independent path length (ΔR_i) values. The Si and Ca atoms at the same distance in the fourth shell were constrained to have the same ΔR_i value (Table 5 and Fig. 5).

DISCUSSION

The crystal chemistry of Sc incorporation at the Y site

Unit-cell parameters measured either by single-crystal and by powder X-ray analysis are in excellent agreement with each other. As inferred by Woodland and Angel (1996a), the regular increase of the length of the unit-cell edge as a function of the Sc content (Fig. 6) suggests that Sc is incorporated at a unique structural site, and substitutes for a smaller cation.

The single-crystal structure refinement confirmed that Sc is incorporated only at the Y site. In fact, the refined site-scattering values (ss) at the X sites [59.9–60.2(1) epfu; Table 3] indicate that Ca is the unique chemical species, whereas those refined at the Y sites correspond to Sc occupancies in excellent agreement with the EMP analysis (Table 3). The very low contents of skiagite component detected during the Mössbauer characterization of the powders are not apparent in the results of the single-crystal structure refinement.

Similar to the unit-cell edge, several geometric parameters change almost linearly along the binary (Fig. 7). However, the available data now allow a detailed modeling of the structural changes resulting from the incorporation of a cation larger than Fe^{3+} at the Y site (0.745 vs. 0.645 Å, for Sc and Fe^{3+}, respectively; $\Delta = 0.10$ Å; Shannon 1976).

The garnet structure is characterized by extensive edge-sharing between the three available polyhedra. Therefore, even when a chemical exchange occurs at a single site, the geometry of the other two sites also changes to provide relaxation. In particular, the Y octahedron shares six out of its twelve edges with six adjacent X dodecahedra, and thus changes in the geometry of the octahedron also affect that of the dodecahedron (and vice versa). Rigid unit modes are forbidden in the garnet structure, and thus relaxation can only be achieved by distortion of the polyhedra and rotation of the tetrahedron (cf. Ungaretti et al. 1995; Merli et al. 1995 for a detailed long-range analysis of structural changes in silicate gar-

nets). As a consequence, relaxation mechanisms mainly involve the relative length of the O-O edges and the variation of α, the rotation angle of the tetrahedron about the $\bar{4}$ axis (Born and Zemann 1964).

The plotting of structural parameters as a function of the unit-cell edge allows comparison of the structural changes occurring in the samples of this work ($\Delta^{[6]}r$ = 0.10 Å) with those occurring in grs–adr solid solutions, where Fe^{3+} substitutes for Al ($\Delta^{[6]}r$ = 0.11 Å). Along the adr–CaSc join, the Y-O distance (Fig. 7a) varies almost linearly, but the increase in the Y-O values (ΔY-O grs–adr = 0.10 Å; ΔY-O adr–CaSc = 0.08 Å) is smaller than expected based on values of the ionic radii and the unit-cell edge. In particular, the higher value of the gradient $\Delta a/\Delta$Y-O (2.4 vs. 2.1) in the adr–CaSc join implies that another polyhedron is increasing in size while Sc enters the Y site.

Inspection of the geometry of the X dodecahedron (Fig. 7b) shows that along the adr–CaSc join relaxation is mainly obtained by a significant lengthening of the X2-O distances, with a rate of lengthening greater than that along the grs–adr join (Fig. 7b). As a result, in spite of the constant X-site population, the difference between the X1-O and the X2-O distance significantly decreases along the grs–adr join, but is almost constant along the adr–CaSc join (Fig. 7c). This latter feature is confirmed by the analysis of the EXAFS data collected at the Ca *K*-edge, which is discussed in detail below. On the contrary, the size of the Z tetrahedron remains roughly constant (Fig. 7d; note that the slightly shorter Z-O distance of the CaSc end-member might derive from a bias in the results of Mill et al. 1977, probably due to different refinement procedures).

If we examine the length of the O-O edges, we find other differences between the two joins. Along the adr–CaSc join, the O-O edges shared between two adjacent X dodecahedra remain constant, whereas the unshared edges lengthen. For grs–adr garnets, the same polyhedral edges decrease significantly and remain constant, respectively (Fig. 7e). For the Y octahedron in adr-CaSc garnets, the O-O edges shared with adjacent X dodecahedra lengthen at nearly the same rate as in the grs–adr join, whereas the unshared edges lengthen less than expected (Fig. 7f). In this way, the octahedral angular variance decreases slightly but significantly [from 1.0(1) to 0.7(1)°^{2}] along the adr–CaSc join. The behavior of the O-O edges of the Z tetrahedron is in line with that observed for the grs–adr join (Fig. 7g). For the shared Z-X edge, the value reported by Mill et al. (1977) for endmember CaSc plots off the trend. These features confirm that no chemical substitution is active at the Z site, and that the Z-site geometry obtained by Mill et al. (1977) is anomalous.

A crucial piece of information on the crystal-chemical behavior of silicate garnets is provided by the α parameter, which describes the rotation of the tetrahedron about the $\bar{4}$ axis (Fig. 8). This parameter is a measure of the changes in the relative size of the polyhedra, because each Z tetrahedron shares two O-O edges with adjacent X dodecahedra, and all its vertices with two X dodecahedra and one Y octahedron. Along the prp–grs join, where the larger Ca^{2+} cation substitutes for Mg^{2+} at the X site, the α parameter decreases from 27.5(1) to 24.6(1)°. The opposite effect is observed across the grs–adr join, where α increases from 24.6(1) to 27.2(1)° (Fig. 8). The same trend is observed along the adr–CaSc join, where α increases further up to 28.8(1)°. The deviation of the Sc-doped pyrope and grossular (circles in Fig. 8; cf. Oberti et al. 2006a) is explained by the presence of larger cations at the Z sites (Mg and Sc, respectively).

The α value observed in $Ca_3Sc_2Si_3O_{12}$ is the highest so far observed in calcium silicate garnets. In calcium garnets, the presence of larger chemical species at the Z site does not increase the tetrahedral rotation; for instance, in kimzeyite, $Ca_3(Zr,Ti)_2(Si,Al,Fe)_3O_{12}$, *a* is 12.397 Å and α is 27.4° (Schingaro et al. 2001), and in katoite, $Ca_3Al_2(O_4H_4)_3$, *a* is 12.570 Å and α is 25.4° (Lager et al. 1987). However, the large α value observed in $Ca_3Sc_2Si_3O_{12}$ corresponds to a geometry of the X and Y polyhedra that is absolutely different from the pyralspite garnets (pyrope,

TABLE 4. EXAFS fit results at the Sc *K*-edge

	$CaSc_{10}$	$CaSc_{30}$	$CaSc_{90}$
[Sc-O]x 6: *R* (Å)	2.057(6)	2.099(4)	2.096(5)
σ_i^2 (Å^2)	0.007(1)	0.006(1)	0.006(1)
[Sc-Ca]x 6, [Sc-Si]x 6: *R* (Å)	3.432(5)	3.432(4)	3.444(5)
σ_i^2 (Å^2)	0.004(1)	0.005(1)	0.005(1)
S_0^2	1.0	1.0	1.0
ΔE_0	2 ± 1	4 ± 1	4 ± 1
R-factor	0.018	0.009	0.010

TABLE 5. EXAFS fit results at the Ca *K*-edge (the corresponding values from single-crystal XRD are included for comparison)

	$CaSc_{10}$	$CaSc_{30}$	$CaSc_{90}$	$CaSc_{100}$
[Ca-O]x 4: R (Å)	2.34(2)	2.34(2)	2.36(2)	
XRD	*2.362*	*2.369*	*2.389*	*2.390*
σ_i^2 (Å^2)	0.003(1)	0.004(1)	0.005(1)	
[Ca-O]x 4: R (Å)	2.48(2)	2.48(2)	2.50(2)	
XRD	*2.501*	*2.509*	*2.526*	*2.532*
σ_i^2 (Å^2)	0.003(2)	0.003(2)	0.003(2)	
[Ca-Si]x 2: R (Å)	3.03(1)	3.04(1)	3.08(1)	
XRD	*3.019*	*3.028*	*3.057*	*3.063*
σ_i^2 (Å^2)	0.004(2)	0.005(1)	0.005(1)	
[Ca-Fe]x 4: R (Å)	3.380(5)	3.377(3)		
XRD	*3.375*	*3.386*		
σ_i^2 (Å^2)	0.004(2)	0.005(1)		
[Ca-Sc]x 4: R (Å)			3.44(1)	
XRD			*3.418*	*3.424*
σ_i^2 (Å^2)			0.005(1)	
[Ca-Si]x 4, [Ca-Ca]x 4: R (Å)	3.709(6)	3.714(4)	3.79(2)	
XRD	*3.697*	*3.709*	*3.744*	*3.751*
σ_i^2 (Å^2)	0.004(2)	0.005(1)	0.005(1)	
[Ca-O]x 4: R (Å)	3.83(2)	3.82(2)	3.84(2)	
XRD				*3.873*
σ_i^2 (Å^2)	0.003(4)	0.003(4)	0.003(2)	
S_0^2	0.6	0.6	0.6	
ΔE_0	4 ± 1	4 ± 1	4 ± 1	
R-factor	0.0022	0.0014	0.0019	

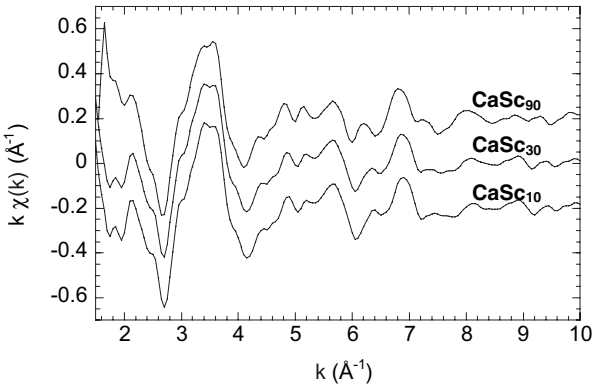

FIGURE 4. Ca *K*-edge EXAFS data.

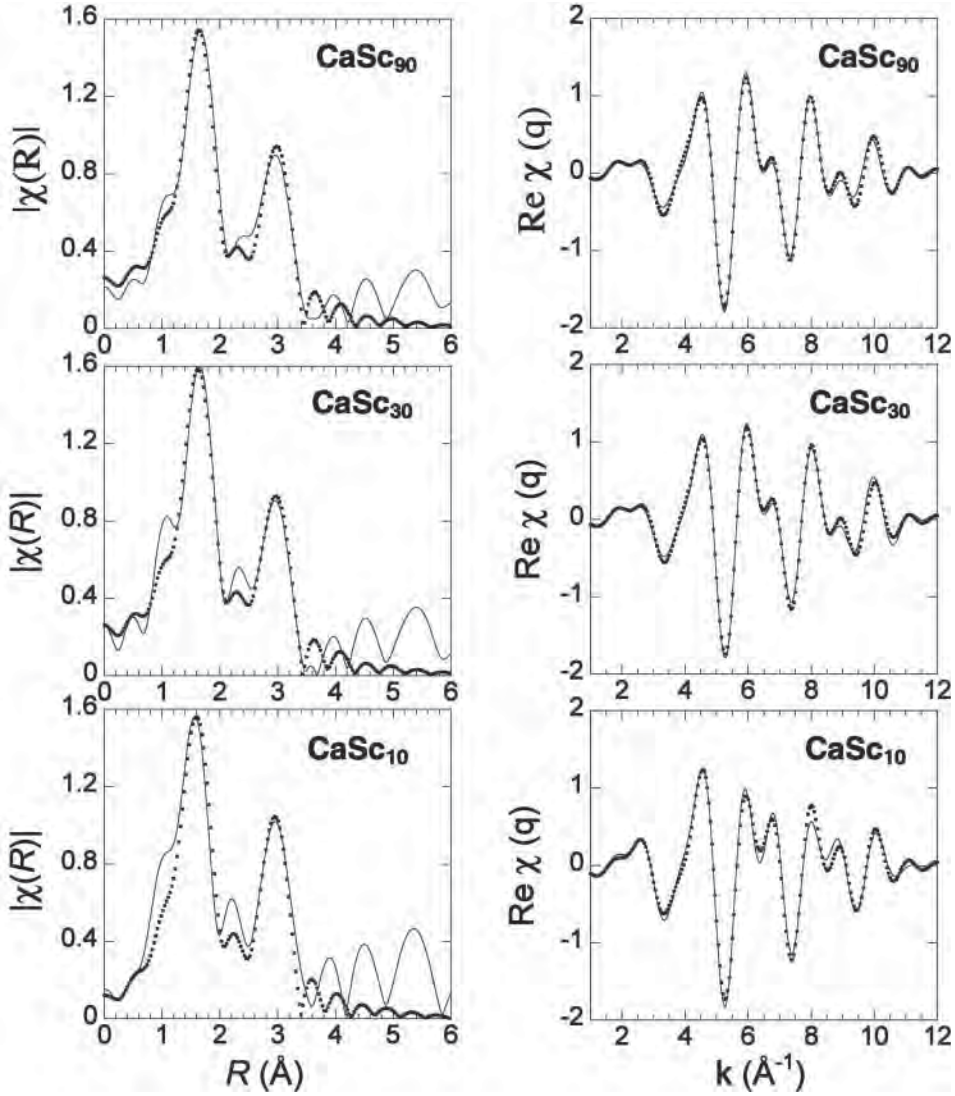

FIGURE 5. Left column: Fourier transform of Ca *K*-edge data (solid line) and fitted signal (dots) (*k*-weight = 2; *k*-range = 3.0–9.8 $Å^{-1}$); right column: inverse-Fourier transform of EXAFS data (solid line) and fitted signal (dots) (1.2 < *R* < 3.4 Å).

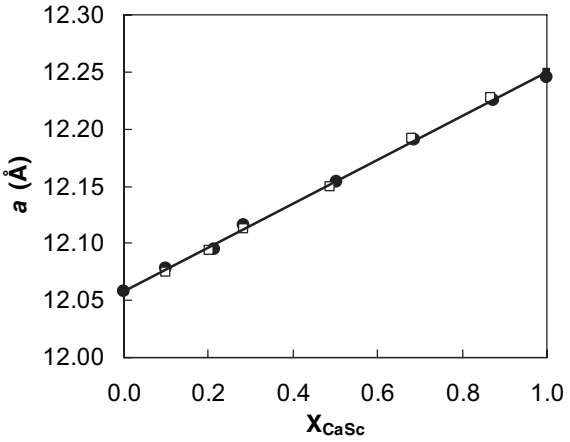

almandine, and spessartine), which couple large α angles with *a* values ranging from 11.45 to 11.62 Å. Even larger α values are to be expected in silicate garnet containing X cations smaller than Ca and Y cations larger than Al. Using the predictive equation provided by Novak and Gibbs (1971), we can calculate the structural features of some of these end-members, most of which are either very rare or not found in nature, or unstable at ambient *P*/*T* conditions. For instance, nominal calderite ($Mn_3^{2+}Fe_2^{3+}Si_3O_{12}$) is predicted to have *a* = 11.840 Å and α = 28.9°, nominal kho-harite ($Mg_3Fe_2^{3+}Si_3O_{12}$) to have *a* = 11.690 Å and α = 30.1°, and

FIGURE 6. Variation of the unit-cell edge along the adr–CaSc join. Empty squares = single-crystal; dots = powders. The line connecting the two end-members (black squares) is drawn to guide the eye.

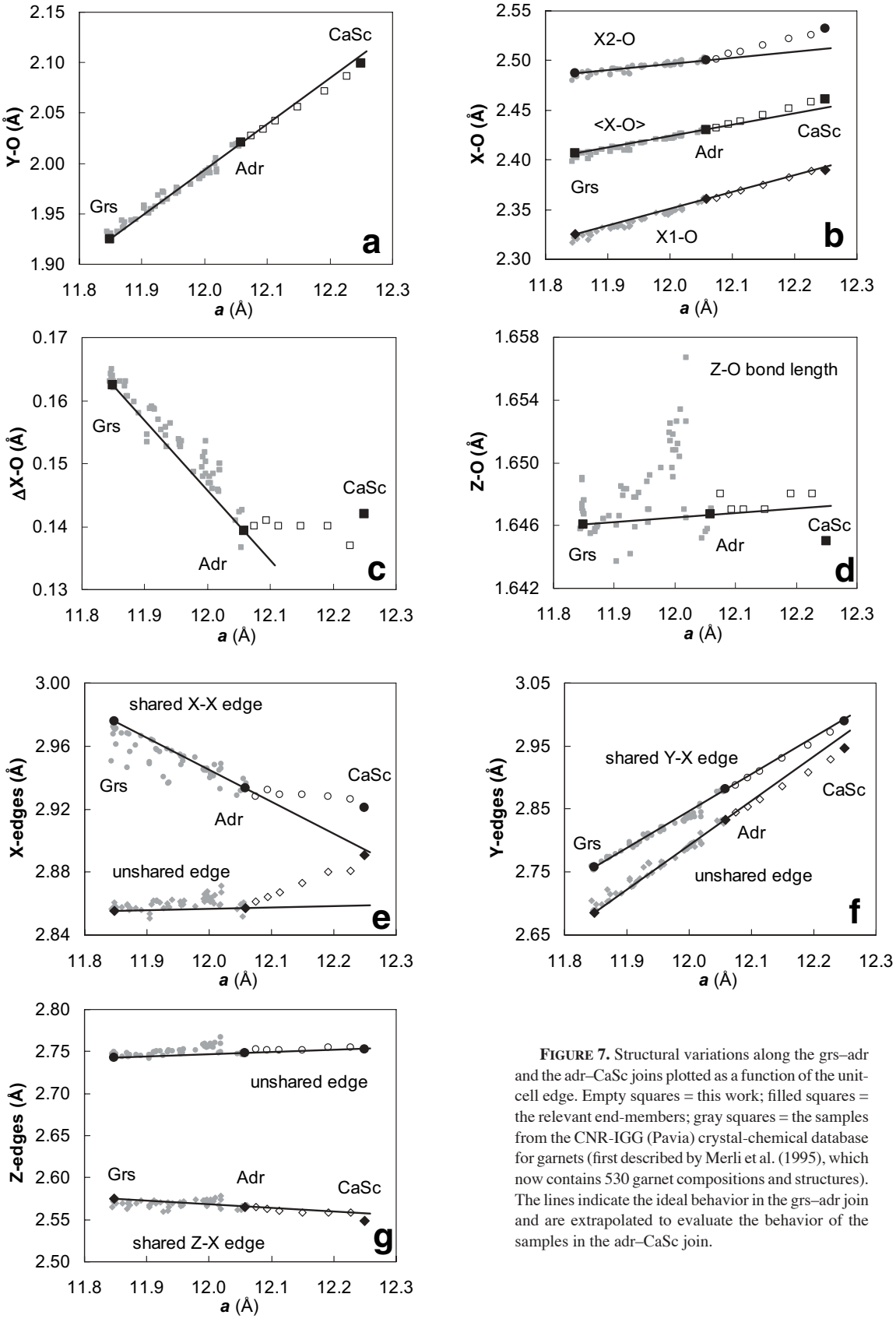

FIGURE 7. Structural variations along the grs–adr and the adr–CaSc joins plotted as a function of the unit-cell edge. Empty squares = this work; filled squares = the relevant end-members; gray squares = the samples from the CNR-IGG (Pavia) crystal-chemical database for garnets (first described by Merli et al. (1995), which now contains 530 garnet compositions and structures). The lines indicate the ideal behavior in the grs–adr join and are extrapolated to evaluate the behavior of the samples in the adr–CaSc join.

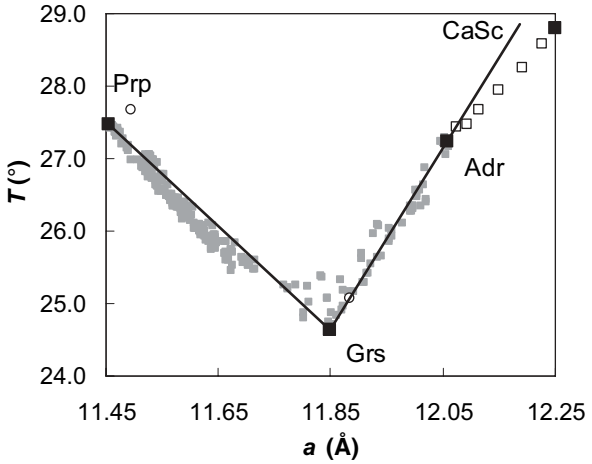

FIGURE 8. Changes in the rotation of the tetrahedron (α) in silicate garnets. Symbols as in Figure 6; circles are the Sc-doped pyrope and Sc-doped grossular of the companion paper (Oberti et al. 2006a).

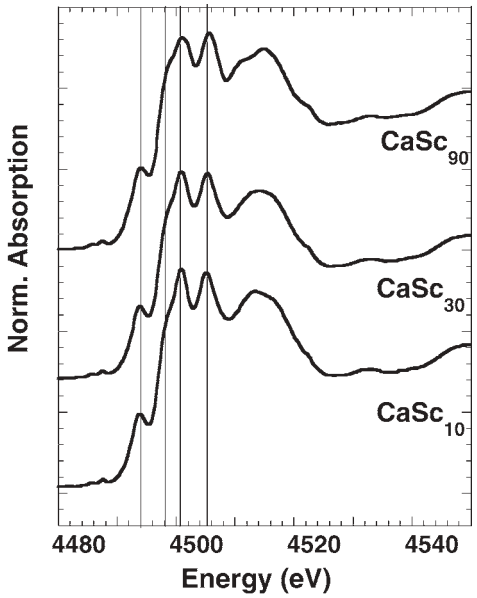

FIGURE 9. XANES spectra collected at the Sc *K*-edge. The individual spectra have been normalized with respect to the high-energy side of the curve.

nominal knorringite ($Mg_3Cr_2Si_3O_{12}$) to have a = 11.640 Å and α = 29.3°. Experimental data are available only for skiagite-rich samples (a is 11.708 Å and α is 29.6° in the 90% $Fe^{2+}_3Fe^{3+}_2Si_3O_{12}$ –10% $Fe_3Al_2Si_3O_{12}$; Woodland and Ross 1994), and in blythite ($Mn^{2+}_3Mn^{3+}_2Si_3O_{12}$; Arlt et al. 1998), where a is 11.788 Å and α is 29.5°.

Results of the XAS analysis

Hints from the Sc *K*-edge. The Sc *K*-edge XANES spectra of the solid-solution terms under investigation are reported in Figure 9; they are ordered from bottom to top as a function of increasing Sc content. The general form of the spectra, the energy positions and the relative intensities of the several clearly resolved features are very similar in the three samples. This is a further strong indication that Sc is hosted in the same crystallographic site in all the samples examined.

The background-subtracted EXAFS data are shown in Figure 2a, and the corresponding Fourier transforms are shown in Figure 2b. Also in this case, only minor changes are observed in both the magnitude and positions of the peaks, which is a further indication of the same local geometry around Sc.

The EXAFS analysis of the first coordination shell of $CaSc_{10}$ provides a Sc-O bond distance slightly shorter (about 2.06 Å) than the "long-range" Sc-O value (about 2.10 Å) determined by SREF on the end-member $Ca_3Sc_2Si_3O_{12}$ (Mill et al. 1977). This suggests that Sc, when present as a very minor species at the Y site in the andradite matrix, adapts itself to a smaller site volume likely imposed by the dominant Fe^{3+}. In contrast, in samples $CaSc_{30}$ and $CaSc_{90}$ the octahedral Sc-O distance is virtually identical to that of the CaSc end-member. Therefore, Sc is able to impose its steric requirements at contents even lower than 0.60 apfu.

This finding confirms the hypothesis, made in the companion paper (Oberti et al. 2006a), that the incorporation of Sc at the Y site is hampered in the most compact garnet structures. In pyrope, where both X and Y sites are occupied by the smallest possible cations, Sc incorporation occurs only at the X site (in Sc-doped pyrope, a = 11.494 Å, α = 27.7°). In the intermediate solid-solution terms and in grossular, where the presence of Ca significantly increases the X site dimension and even changes the coordination geometry of the X cation (Oberti et al. 2006b), Sc partitions itself between the X, Y, and Z sites, so that an increase in the Y site dimension couples with an increase in the Z site dimension (in Sc-doped grossular, a = 11.883 Å, α = 25.1°). In any case, the size of the dominant Y cation (Al, with $^{[6]}r$ = 0.535 Å) prevents Sc contents beyond 0.20 apfu (i.e., 10% occupancy). From XAS analysis, we could estimate that the octahedral Sc-O distance in Sc-doped grossular is smaller or equal to that observed in $CaSc_{10}$, i.e., 2.06 Å, as discussed in more detail in the companion paper (Oberti et al. 2006a).

Hints from the Ca *K*-edge. EXAFS measurements were also done on the same samples at the Ca *K*-edge (Fig. 4). Ca is the only dodecahedral cation in all the samples studied, hence the structural results from XAS must be directly compared with those obtained by XRD (Table 3). The results of high-quality multi-shell fits (done using Ca-Fe paths for $CaSc_{10}$ and $CaSc_{30}$ and Ca-Sc paths for $CaSc_{90}$) are reported in Figure 5 and Table 5, and are in excellent agreement with the trends evidenced by the XRD study. Notably, the first-shell Ca-O distances are shorter in the low-Sc than in the high-Sc samples: Ca1,2-O are 2.34(2) and 2.48(2) Å in $CaSc_{10}$ and 2.36(2) and 2.50(2) Å in $CaSc_{90}$, with Δ fixed at 0.14 Å in all the samples. The values obtained by single-crystal structure refinement are 2.362(1) and 2.501(1) for $CaSc_{10}$ and 2.389(1) and 2.526(1) for $CaSc_{90}$, with Δ equal to 0.139 and 0.137 Å, respectively. The X1-O and X2-O values refined by Mill et al. (1977) on $Ca_3Sc_2Si_3O_{12}$ are even larger (2.390 and 2.532 Å, Δ = 0.142 Å; Table 3), thus confirming that the Ca-O distances are dependent on the overall garnet composition. Even more significant Sc-dependent differences are observed in the higher-shell coordination geometries around calcium. In particular, the Ca-(Fe,Sc), Ca-Si, and Ca-Ca

bond distances strongly increase going from $CaSc_{10}$ to $CaSc_{90}$, in agreement with the results from diffraction reported in Table 3 (X-Y, X-Z, and X-X, respectively).

It is also important to note that EXAFS short-range data confirms that ΔX-O remains roughly constant along the adr–CaSc join, as shown by long-range information in Figure 7c. This has implications for the neighboring Y-sites since there is extensive edge-sharing between the dodecahedral and octahedral polyhedra and next-nearest neighbor effects are known to be significant (e.g., Woodland and Ross 1994; Oberti et al. 2006b). Thus, the similar X-site geometries in the adr–CaSc garnets are consistent with the constant quadrupole splitting values of Fe^{3+} observed in the Mössbauer spectra, implying that the local electric charge density about the Fe atoms remains unchanged across the join.

CONCLUDING REMARKS

The general conclusion of this work is that the study of solid-solution behavior of garnet is a rather complicated matter, which must be performed by means of a complete structural and spectroscopic characterization. Apparently ideal behavior of the unit-cell parameter can mask, similar to the present case, complex structural variations. More importantly, the local environment of a given cation in a given site strongly depends on the site population of the other sites, and changes in local environments are not necessarily linear. XAS analysis often reveals differing behavior across different binary joins that may be explained by constraints determined by the garnet matrix. Across the pyrope-grossular join, Ca at the X site changes its coordination from an almost regular [8]-fold coordination in pyrope-dominant compositions to a [4+4]-fold coordination with Δ = 0.15–0.16 Å in grossular dominant compositions (Oberti et al. 2006b). In andradite–$Ca_3Sc_2Si_3O_{12}$ solid solutions, the Ca1-O and Ca2-O distances increase with Sc content, but their difference remains almost constant (Δ = 0.14 Å). In these garnets, the octahedral Sc-O distances are ~2.06 Å for the $adr_{90}CaSc_{10}$ composition, but they jump to ~2.099 Å in the solid solutions containing 30 to 100% of the $Ca_3Sc_2Si_3O_{12}$ component. In terms of Fe^{3+}, the constancy in the hyperfine parameters across the join indicates that the chemical environment of Fe^{3+} is unchanged, in spite of this jump in Y-O bond distance.

After the submission of this paper, the occurrence of a natural scandium garnet with formula $(Ca_{2.97}Mg_{0.02}Y_{0.01})_{\Sigma 3}(Fe^{3+}_{0.663}Zr_{0.584}Ti^{4+}_{0.294}Sc_{0.153}Cr_{0.152}Mg_{0.094}Fe^{2+}_{0.04}Hf_{0.008}V_{0.003})_{\Sigma 2}(Si_{1.898}Al_{0.420}Ti^{4+}_{0.359}Fe^{3+}_{0.323})_{\Sigma 3}O_{12}$, was reported by Galuskina et al. (2005) in an aposkarn achtarandite-bearing rodingite-like rock in Sakha-Yakutia, Russia. It will be interesting to compare in detail the crystal structure of this natural garnet, when available, with the structural data of our synthetic phases.

ACKNOWLEDGMENTS

The high-pressure syntheses and powder X-ray diffraction work were performed at the Bayerisches Geoinstitut under the EC "Human Capital and Mobility—Access to Large Scale Facilities" program (contract no. ERBCHGEC940053 to D.C. Rubie). Ross Angel graciously performed the refinements of the powder diffraction data. H.P. Meyer (Heidelberg) is thanked for helping with the microprobe standardization. Catherine McCammon is thanked for access to the Mössbauer spectrometers in Bayreuth. The paper benefited from the comments of Evgeny V. Galuskin and George Lager.

REFERENCES CITED

Arlt, T., Armbruster, T., Miletich, R., Ulmer, P., and Peters, T. (1998) High-pressure single-crystal synthesis, structure, and compressibility of the garnet $Mn^{2+}_3Mn^{3+}_2[SiO_4]_3$. Physics and Chemistry of Minerals, 26, 100–106.

Amthauer, G., Annesten, H., and Hafner, S.S. (1976) The Mössbauer spectrum of ^{57}Fe in silicate garnets. Zeitshrift fur Kristallographie, 143, 14–55.

Ankudinov, A.L., Ravel, B., Rehr, J.J., and Conradson, S.D. (1998) Real space multiple scattering calculation of XANES. Physical Reviews B, 58, 7565–7576.

Born, L. and Zemann, J. (1964) Abstandsberechnungen und gitterenergetische Berechnungen an Granaten. Beiträge zur Mineralogie und Petrographie, 10, 2–23.

Galuskina, I.O., Galuskin, E.V., Dzierzanowski, P., Armbruster, Th., and Kozanecki, M. (2005) A natural scandium garnet. American Mineralogist, 90, 1688–1692.

Ito, J. and Frondel, C. (1968) Synthesis of the scandium analogues of aegirine, spodumene, andradite, and melanotekite. American Mineralogist, 53, 1276–1280.

Lager, G.A., Armbruster, Th., and Faber, J. (1987) Neutron and X-ray diffraction study of hydrogarnet $Ca_3Al_2(O_4H_4)_3$. American Mineralogist, 72, 756–765.

Larson, A.C. and Von Dreele, R.B. (1997) GSAS: General Structure Analysis System. Document LAUR 86-748, Los Alamos National Laboratory.

Merli, M., Callegari, A., Cannillo, E., Caucia, F., Leona, M., Oberti, R., and Ungaretti, L. (1995) Crystal-chemical complexity in natural garnets: structural constraints on chemical variability. European Journal of Mineralogy, 7, 1239–1249.

Mill, B.V., Belokoneva, E.L., Simonov, M.A., and Belov, N.V. (1977) Refined crystal structures of the scandium garnets $Ca_3Sc_2Si_3O_{12}$ and $Cd_3Sc_2Ge_3O_{12}$. Zhurnal Strukturnoi Khimii, 18, 399–402.

Newville, M. (2001) IFEFFIT: interactive XAFS analysis and FEFF fitting. Journal of Synchrotron Radiation, 8, 322–324.

Novak, G.A. and Gibbs, G.V. (1971) The crystal chemistry of silicate garnets. American Mineralogist, 56, 791–825.

Oberti, R., Quartieri, S., Dalconi, M.C., Boscherini, F., Iezzi, G., Boiocchi, M., and Eeckhout, S. (2006a) Site preference and local geometry of Sc in garnets: I. Multifarious mechanisms in the pyrope-grossular join. American Mineralogist, 91, 1230–1239.

——— (2006b) Distinct local environments for Ca along the non-ideal pyrope-grossular solid-solution: a new model based on crystallographic and EXAFS analysis. Chemical Geology, 225, 347–359.

Pouchou, J.L. and Pichoir, F. (1985) "PAP" φ(ρZ) procedure for improved quantitative microanalysis. In J.T. Armstrong, Ed., Microbeam Analysis 1985, The 20th Annual Conference of the Microbeam Analysis Society, p. 104–160. San Francisco Press.

Ravel, B. and Newville, M. (2005) ATHENA, ARTEMIS, HEPHAESTUS: Data Analysis for X-ray absorption spectroscopy using IFEFFIT. Journal of Synchrotron Radiation, 12, 537–541.

Schingaro, E., Scordari, F., Capitanio, F., Parodi, G., Smith, D.C., and Mottana, A. (2001) Crystal chemistry of kimzeyite from Anguillara, Mts. Sabatini, Italy. European Journal of Mineralogy 13, 749–759.

Shannon, R.D. (1976) Revised effective ionic radii and systematic studies of interatomic distances in halides and chalcogenides. Acta Crystallographica, A32, 751–767

Sheldrick, G.M. (1996) SADABS. Siemens Area Detector Absorption Correction Program. University of Göttingen, Germany.

Toby, B.H. (2001) EXPGUI, a Graphical User Interface for GSAS. Journal of Applied Crystallography, 34, 210–213.

Ungaretti, L., Leona, M., Merli, M., and Oberti, R. (1995) Non-ideal solid solution in garnet: crystal-structure evidence and modeling. European Journal of Mineralogy, 7, 1299–1312.

Woodland, A.B. and Angel, R.J. (1996a) Incorporation of Sc in garnet and the properties of $Ca_3Fe_2Si_3O_{12}$–$Ca_3Sc_2Si_3O_{12}$ garnet solid solutions. EOS Transactions of the American Geophysical Union, 77, F829.

——— (1996b) Synthesis and properties of $Ca_3Fe_2Si_3O_{12}$–$Ca_3Sc_2Si_3O_{12}$ garnet solid solutions. Terra Abstracts, 8, 68.

Woodland, A.B. and O'Neill, H.St.C. (1995) Phase relations between $Ca_3Fe^{3+}_2Si_3O_{12}$–$Fe^{2+}_3Fe^{3+}_2Si_3O_{12}$ garnet and $CaFeSi_2O_6$–$Fe_2Si_2O_6$ pyroxene solid solutions. Contribution to Mineralogy and Petrology, 121, 87–98.

Woodland, A.B. and Ross, C.R., II (1994). A crystallographic and Mössbauer-spectroscopy study of $Fe^{2+}_3Al_2Si_3O_{12}$–$Fe^{2+}_3Fe^{3+}_2Si_3O_{12}$, (almandine–skiagite) and $Ca_3Fe^{3+}_2Si_3O_{12}$–$Fe^{2+}_3Fe^{3+}_2Si_3O_{12}$ (andradite–skiagite) garnet solid-solutions. Physics and Chemistry of Minerals, 21, 117–132.

MANUSCRIPT RECEIVED JULY 18, 2005
MANUSCRIPT ACCEPTED APRIL 10, 2006
MANUSCRIPT HANDLED BY MARC HIRSCHMANN